A review of X-ray absorption near-edge spectroscopic studies of pyrochlore-type oxides proposed for nuclear materials applications

Esther Rani Aluri, Andrew P. Grosvenor*

Department of Chemistry, University of Saskatchewan, Saskatoon, SK, Canada, S7N 5C9

* Author to whom correspondence should be addressed

E-mail: andrew.grosvenor@usask.ca

Phone: (306) 966-4660

Fax: (306) 966-4730

Abstract:

Pyrochlore-type oxides ($A_2B_2O_7$) have received considerable attention for nuclear waste sequestration applications because of the compositional diversity and structural flexibility of these materials. It is important to understand how the electronic structure of these materials changes depending upon composition and to study the radiation tolerance of these materials. X-ray absorption near-edge spectroscopy (XANES) can be used to investigate the electronic structure, oxidation state, bonding environment, and local coordination environment of the absorbing atom. The objective of this contribution is to demonstrate how XANES can be used to effectively study pyrochlore-type oxide materials for nuclear material applications.

Keywords: Anti-site disorder; Coordination number; Nuclear waste; Oxidation state; Pyrochlore-type oxides; Radiation damage; sequestration; Synchrotron Radiation; XANES

Introduction

Nuclear energy is considered a clean energy source that provides large amounts of energy that can meet industrial and societal energy needs.[1-5] Nuclear power plants produced ~12% of world's energy in 2012.[6] However, the nuclear industry has produced, and continues to produce, a significant amount of radioactive nuclear waste. For example, the accumulated nuclear waste from spent nuclear fuel (measured by volume) and uranium mill tailings were 9079 m^3 and 214,000,000 tonnes, respectively, in Canada to the end of 2010.[7]

A number of nuclear wasteforms have been proposed to immobilize nuclear waste from spent nuclear fuel, including ceramic oxides.[8,9,10,11,12] Nuclear wasteforms are materials that can safely and securely incorporate various radioactive nuclear waste elements. A key concern of nuclear wasteform materials is the long-term stability and durability of these materials, which may be affected by the radioactive decay of incorporated nuclear waste elements.[12,13,14,15,16,17,18] During the radioactive decay (i.e., α- or β-decay) process, the incorporated radioactive nuclear waste elements may release α- or β-particles over a period of time and transform to daughter products. These events can damage the structure of a nuclear wasteform through various processes. The decay of incorporated radioactive elements can lead to the swelling of the structure and the development of crystal defects.[8] A change in the structure of a material because of radiation damage can affect its ability to restrict the mobility of contained radioactive waste elements.[8] Studying how a proposed nuclear wasteform responds to the radioactive decay of incorporated nuclear waste elements is a crucial step to the development of these materials.

Ceramic materials have been proposed as nuclear wasteforms as the naturally occurring mineral analogues can contain actinides and many remain crystalline (or partially crystalline)

over millions of years.[19,20,21,22,23,24] A number of chemically durable, stable, and flexible ceramic materials have been proposed as potential nuclear wasteforms such as zirconolite ($CaZrTi_2O_7$), monazite ($(Ce,La,Nd,Th)PO_4$), hollandite ($BaAl_2Ti_6O_{16}$), Zircon ($ZrSiO_4$), perovskite (ABO_3; A and B are cations occupied in different atomic positions of crystal structure), fluorite (AO_2), and pyrochlore ($A_2B_2O_7$).[15,16,19,24,25] Multi-phase ceramic materials like Synroc (i.e., synthetic rock), have also been designed to incorporate a wide range of complex nuclear waste elements.[19,25,26,27,28,29] Various forms of Synroc have been developed to immobilize nuclear waste elements including pyrochlore-type oxide (e.g., $(Ca,Gd,U,Pu,Hf)_2Ti_2O_7$) enriched Synroc (Synroc-F), which has been developed for the disposal of nuclear waste from CANDU (Canada deuterium uranium) reactors.[19,29,30,31,32] This multi-phase material has been observed to be efficient for the immobilization of nuclear waste with a loading of 50 wt % U/PuO_2.[19,29,32,33]

The pyrochlore-type crystal structure, which is the focus of this contribution, shows remarkable compositional diversity with over 500 compositions being known.[34,35] The diverse chemistry of pyrochlore-type oxides has resulted in these materials having a range of technological applications such as catalysis, piezoelectricity, ferro- and ferri-magnetism, luminescence, giant magneto resistance, and ionic conductivity.[36,37,38,39,40,41] The advantages of using pyrochlore-type oxides as nuclear wasteforms are the high compositional diversity, structural flexibility, chemical durability, and resistance to radiation induced damage of these materials.[16,25,34,35,42,43] The pyrochlore-type crystal structure ($A_2B_2O_7$; space group: $Fd\bar{3}m$) is related to the fluorite structure (AO_2, space group: $Fm\bar{3}m$); however, it has two cation sites (vs. one in the fluorite structure) and one eighth fewer oxygen ions.[16,34,35,42] The pyrochlore-type structure is shown in Figure 1.[44] The A-site cations (A = La to Lu, Ca, Y, etc) are generally trivalent while the B-site cations (B = Ti, Sn, Ta, Zr, Hf, etc.) are tetravalent. It is also possible

for the A- and B-site cations to have oxidation states other than 3+ and 4+, respectively.[16,34,42,45] The A-site cations are in an eight coordinate-site within a distorted cubic polyhedra and the B-site cations occupy a distorted octahedral environment. The structure has three distinct oxygen anion sites within tetrahedral interstices and one of the anion sites is vacant when the pyrochlore structure is perfectly ordered.[42,46] The local environments for each oxygen anion site are OA_4, OB_4, and OA_2B_2.

<Figure 1 near here>

Anti-site disorder can occur among cation and anion sites in pyrochlore-type oxide materials depending on composition and the method used to synthesize these materials.[47,48] Anti-site disorder can also be driven by thermal treatment, the application of an external pressure, or implanting the material with an ion beam.[47,49,50] The driving force for the degree of cation anti-site disorder is generally dependant on the ratio of the A- and B-site ionic radii (r_A/r_B). As the ionic radius ratio (r_A/r_B) decreases and approaches ~1.46, the ordered pyrochlore structure can transform to the defect fluorite structure (i.e., order-disorder phase transition) through the disordering of A- and B-site cations.[16,48,50,51] Other factors, such as the covalency of the metal-oxygen bonds and the electronic structure of the material, can also influence the transformation of the ordered pyrochlore-type structure to the disordered defect fluorite-type structure.[16,52,53,54]

Pyrochlore-type oxides ($A_2B_2O_7$) have received considerable attention for nuclear waste sequestration applications. It is important to understand how the electronic structure of these materials changes depending on composition and how the structure of these materials is affected by radiation. X-ray absorption near-edge spectroscopy (XANES) is a powerful technique that can be used to study the electronic structure of the materials as well as the effect of radiation induced structural damage on these materials. The objective of this contribution is to

demonstrate how XANES can be used to extract important information on pyrochlore-type oxides, including: oxidation state, coordination number (CN), anti-site disorder, and the effect of radiation on the structure of the material.

An overview of XANES

XANES spectra are collected using X-rays from a synchrotron radiation facility. The absorption of an X-ray photon by an atom can result in the excitation of a core electron into unoccupied atomic/molecular orbitals above the Fermi level (i.e., conduction and/or continuum states). XANES is element specific and sensitive to the oxidation state, bonding environment, and local geometry around the absorbing atom.[55,56,57,58,59] The absorption process mainly follows dipole selection rules (i.e., $\Delta l = \pm 1$); however, quadrupolar transitions (i.e., $\Delta l = \pm 2$) can also be observed in some circumstances. The focus of this contribution has been placed on studying materials using K-edge XANES spectra (excitation of 1s electrons) and L-edge XANES spectra (excitation of 2p electrons).[55,56,57,58,59] A schematic diagram for representative K-edge and L-edge transitions are shown in Figure 2. The L_1-edge consists of 2s→np transitions whereas the $L_{2,3}$-edge consists of 2p→ns/(n-1)d transitions. The most prominent transitions in K-edge spectra are from dipolar transitions (1s→np) but the observation of quadrupolar transitions (1s→(n-1)d) in the spectra is also possible.[55,56,57,58,59] For example, Ti K-edge XANES spectra (cf. Figure 3) consist of a low intensity pre-edge (A) feature (1s→3d; quadrupolar transitions) and a higher intensity main edge (B,C) feature (1s→4p; dipolar transitions). The weak intensity pre-edge region (A) probes the d-states of a transition metal and is sensitive to the chemical environment.[60,61,62,63] The intensity of pre-edge peaks can be increased by the addition of dipolar character through the overlap of d- and p-states. This p-d mixing can result from varying the

coordination environment (e.g., octahedral to tetrahedral geometry) of the absorbing atom or a distortion of the coordination environment.[60,61,62,63] As illustrated in Figure 3a, decreasing the coordination number ($Ti^{[6]} \rightarrow Ti^{[5]} \rightarrow Ti^{[4]}$) can result in an increase in the intensity of the pre-edge feature (A). Further, the absorption energies of the pre-edge and main-edge peaks are sensitive to the oxidation state and CN of the absorbing atom (see Figure 3b).[60,61,62,63,64]

<Figure 2 near here>

<Figure 3 near here>

Examples of how XANES can be used to study the local structure and electronic structure of pyrochlore-type oxides

Identifying oxidation states, bonding, and CN changes in pyrochlore-type oxides depending on composition

A unique advantage of using XANES to study materials is the ability of this technique to provide information on the local electronic structure of specific elements and to provide direct information on the effect of composition, structure, and synthetic method on oxidation state, CN, and bonding. XANES studies of $Yb_2Ti_{2-x}Fe_xO_{7-\delta}$ and $Gd_2Ti_{2-x}Sn_xO_7$ are discussed below as an example of this utility.[65,66] $Yb_2Ti_2O_7$ has a large number of applications due to its remarkable chemical and physical properties. Some of these properties (*e.g.*, ionic conduction) can be improved by introducing oxygen vacancies. It has been proposed that substitution of Fe into the B-site could affect the ionic conductivity of these materials; however, this would require that Fe adopt a 3+ oxidation state and that it preferentially substitutes for Ti^{4+} in the 6-coordinate B-site.[67] The application of XANES to study this system has allowed for this information to be determined.[65]

The Fe K-edge spectra from $Yb_2Ti_{2-x}Fe_xO_{7-\delta}$ are shown in Figure 4. The intensity of the pre-edge peak was observed to increase as Fe was substituted for Ti and is a result of a decrease in CN.[65] The intense main-edge region (B and C in Figure 4) can shift because of changes in CN and oxidation state.[62,68] Feature B (and C) can shift to higher energy with increasing oxidation because of reduced screening of the nuclear charge. Fewer electrons are available to screen the nuclear charge with increasing oxidation state, requiring more energy to remove core electrons. Feature B can also shift because of a change in CN because of changes in the magnitude of final state relaxation that can occur as a result of a change in CN. The lower the CN, the more final state relaxation that occurs which results in a lower absorption energy.[62,69] Feature C results from a dipolar transition of 1s electrons to 4p states that are hybridized with O 2p states and changes with CN.[62,68] As the CN decreases, the number of Fe 4p-O 2p final states available for 1s electrons to be excited to also decreases, resulting in a decrease in the intensity of feature C.[62,68,70,71]

The oxidation state of Fe in $Yb_2Ti_{2-x}Fe_xO_{7-\delta}$ can be determined by comparing the Fe K-edge spectra to those from perovskite-type $La_{1-x}Sr_xFeO_{3-\delta}$ materials (Figures 4 and 5), which contain Fe^{3+} and/or Fe^{4+} depending on the Sr concentration.[72] The pre-edge peak (feature A) in the Fe K-edge spectra from $La_{1-x}Sr_xFeO_{3-\delta}$ was observed to shift by ~+0.5 eV as Sr^{2+} was substituted for La^{3+} (Figure 5) because of the increased oxidation state of Fe (from Fe^{3+} to Fe^{4+}).[65] The centroid of the pre-edge peak for all $Yb_2Ti_{2-x}Fe_xO_{7-\delta}$ compositions was in good agreement with that for $LaFeO_3$ (cf. Figure 5), implying that all Fe ions have a 3+ oxidation state in the $Yb_2Ti_{2-x}Fe_xO_{7-\delta}$ system. As has been explained earlier, the increase in intensity of feature A and the decrease in intensity of feature C in the Fe K-edge spectra from $Yb_2Ti_{2-x}Fe_xO_{7-\delta}$ (Figure 4) with increasing Fe incorporation implies that the Fe CN decreases. The shift of feature

B to lower energy with increasing Fe content is also a result of a decrease in the CN of Fe with increasing Fe content.[65] This study confirmed that: (1) Fe adopts a 3+ oxidation state in $Yb_2Ti_{2-x}Fe_xO_{7-\delta}$; (2) Fe substitutes into the B-side as the pre-edge peak intensity and energy is most similar to that of 6-coordinate Fe when the Fe concentration is low in these materials; and (3) $Yb_2Ti_{2-x}Fe_xO_{7-\delta}$ is oxygen deficient as the pre-edge peak intensity increased with greater Fe incorporation indicating that the B-site CN decreases with Fe substitution, which would require the presence of O vacancies.[65]

<Figure 4 near here>

<Figure 5 near here>

XANES can also be used to study how changes in composition can influence the electronic structure, including bond covalency, of pyrochlore-type oxides, which is demonstrated below through the examination of $Gd_2Ti_{2-x}Sn_xO_7$ materials.[66] The Ti K-edge spectra from $Gd_2Ti_{2-x}Sn_xO_7$ are presented in Figure 6 and compare well to K-edge XANES spectra from 6-coordinate Ti^{4+}.[65,73] Three features (A_1, A_2 and A_3) are observed in the pre-edge region and result from both local and non-local excitations.[73,74,75] Feature A_1 in the pre-edge region results from pure local 1s→3d-t_{2g} excitations. The low energy region of feature A_2 results from local 1s→3d-e_g^* excitations, while the higher energy region results from non-local (intersite-hybrid) excitations of 1s electrons to d- states of next-nearest neighbour atoms that overlap with Ti 4p states of the absorbing atom *via* O 2p states.[74] Feature A_3 is a result of pure non-local (intersite-hybrid) excitations.[74,75]

The intensity of feature A_1 was found to be invariant with Sn substitution in $Gd_2Ti_{2-x}Sn_xO_7$ (Figure 6a); however, the intensities of features A_2 and A_3 were observed to

change considerably.[66] The intensity of pre-edge features resulting from local excitations (e.g., A_1; low energy side of A_2) can change because of changes in CN or distortion of the local coordination environment.[73,76,77] The intensity of feature A_1 was not observed to change with change in composition indicating that the Ti CN remains nearly constant in this system, which follows with previous studies that have found limited anti-site disorder in these materials.[54,78] However, the intensities of feature A_3 and the high-energy side feature A_2 changed with a variation in composition.[74,79] The decrease in intensity of these two features with greater Sn content is related to the concentration of unoccupied next-nearest neighbour d orbitals.[79] As Sn is substituted for Ti, fewer unoccupied next nearest neighbour Ti 3d states are available for 1s electrons from the absorbing atom to be excited to, resulting in a decrease in the intensity of these features.

The main-edge energy (feature B) was observed to shift to higher energy with greater Sn incorporation $Gd_2Ti_{2-x}Sn_xO_7$ (Figure 6b), which could result from both ground-state and final state effects.[66] Final-state effects occur due to the relaxation of electrons towards the core-hole produced during the excitation and are sensitive to changes in the chemical environment.[69,80] For example, a lower CN results in greater final state relaxation effects due to the presence of fewer electrons in the first coordination shell that are available to screen the core-hole.[62,69] Ground-state effects, on the other hand, mainly occur due to changes in the charge and bonding environment of the absorbing atom, leading to a change in the screening of the nuclear charge of the absorbing atom. For example, feature B could shift to higher energy due to the development of a more positive charge on Ti with greater Sn substitution in $Gd_2Ti_{2-x}Sn_xO_7$ as Sn is more electronegative than Ti ($\chi_{Sn} = 1.8 > \chi_{Ti} = 1.5$).[81]

The partial density of states (DOS) from $Y_2Ti_{2-x}Sn_xO_7$ were calculated to confirm if the shifts observed in the Ti K-edge XANES spectra from $Gd_2Ti_{2-x}Sn_xO_7$ result from final-state or ground-state effects (Figures 7). (The intensity and absorption energy of the features found in the Ti K-edge spectra from the $Y_2Ti_{2-x}Sn_xO_7$ series vary with Sn composition in a similar fashion to those observed in the spectra from $Gd_2Ti_{2-x}Sn_xO_7$.[66]) The calculated Ti 3d and 4p conduction states shown in Figure 5 are involved in Ti-O anti-bonding interactions. The small negative shift in energy observed for the Ti 3d partial DOS (~ -0.3 eV) and the significant shift to higher energy observed for the Ti 4p partial DOS (~ +0.8 eV) with greater Sn content is in agreement with the Ti K-edge XANES spectra from $Gd_2Ti_{2-x}Sn_xO_7$ (c.f. Figures 6 and 7). The DOS calculations confirmed that ground-state effects are primarily responsible for the changes observed in the spectra reported in this study, as the effect of a core-hole (i.e., final-state effects) was not considered in the calculations. As the Sn content increases in $Gd_2Ti_{2-x}Sn_xO_7$, the more covalent Sn-O interaction leads to an increase in the ionic strength of the Ti-O bond to ensure charge balance, as Sn is more electronegative than Ti.[81] As the ionic character of the Ti-O bond increases with greater Sn content, a more positive charge develops on Ti. This results in a reduced ground-state screening of the nuclear charge and is observed as a shift to higher energy with greater Sn incorporation of region B in the Ti K-edge XANES spectra.[79] Whereas the previous example demonstrated the usefulness of comparing XANES spectra to those from standard materials to aid in interpretation, this example demonstrates the usefulness of using theory to aid in the interpretation of XANES spectra.

The Sn L_3-edge spectra from the $Gd_2Ti_{2-x}Sn_xO_7$ series were also collected in this study to probe the effects of covalency on Sn as the composition was varied (Figure 8).[66] The Sn L_3-edge spectra displayed two features that resulted from $2p_{3/2} \rightarrow 5s$ (Feature A) and $2p_{3/2} \rightarrow 5d$ (Feature B)

excitations.[82,83,84] The intensity of feature B decreased with greater Sn incorporation in the $Gd_2Ti_{2-x}Sn_xO_7$ system. The observed decrease in intensity was attributed to the increased covalency of the Sn-O bond as Sn was substituted for Ti.[66] With increasing covalency of the Sn-O bond, the Sn 5d states share more electrons with the O 2p states, which results in fewer unoccupied Sn 5d states being available for Sn 2p electrons to be excited to and leads to a decrease in intensity of feature B in the spectra with increasing Sn content.

<Figure 6 near here>

<Figure 7 near here>

<Figure 8 near here>

Experimental considerations when using XANES to study local disorder

The amount of cation antisite disorder that occurs in pyrochlore-type oxides depending on composition has been investigated in the past with somewhat conflicting results.[85,86,87] For example, analysis of powder X-ray diffraction data from the $Gd_2Ti_{2-x}Zr_xO_7$ system suggested that Ti and Zr can increasingly occupy the A-site with greater Zr incorporation.[86,87] However, an examination of Ti $L_{2,3}$- and O K-edge XANES spectra instead suggested that Ti remained in the B-site and that only Zr and Gd underwent antisite disorder as the Zr concentration increased.[85] Owing to the difficulty in assigning site occupancies to three different cations across two crystallographically different sites by Rietveld analysis of powder X-ray diffraction data, it can be difficult (although not impossible) to study anti-site disorder by XRD. With respect to the $Gd_2Ti_{2-x}Zr_xO_7$ system, the presence of Ti in the B site with Zr and Gd being disordered across the A and B sites can be rationalized by comparing the ionic radii of the smaller Ti^{4+} ions to the

larger Zr^{4+} and Gd^{3+} ions, as cation antisite disorder generally occurs when the A- and B-site ions are closer in size.[42,88] Knowledge of the local structure is invaluable when investigating how the incorporation of actinides influences the properties and structural stability of these material over time.

The Ti K-edge XANES spectra were collected from $Gd_2Ti_{2-x}Zr_xO_7$ materials and are presented in Figure 9.[89] The shape of the pre-edge regions of the spectra from the $Gd_2Ti_{2-x}Zr_xO_7$ materials remained relatively constant as x increased from 0 to ~1 and are similar to that expected for Ti in a six-coordinate environment. These results are in agreement with multiple studies of these materials.[77,85,90]

Similar to Ti K-edge XANES spectra, Zr K-edge XANES spectra exhibit pre-edge and main-edge features that are a result of 1s→4d (≤ 18005 eV) and 1s→5p (≥ 18005 eV) transitions, respectively.[91,92] Unlike in the Ti K-edge spectra, these regions are not clearly defined in the Zr K-edge spectra, which is a result of: 1) the reduced separation between 4d and 5p states compared to between 3d and 4p states, and 2) the resolution of XANES spectra decreasing with increasing excitation energy because of core-hole lifetime effects, among other reasons.[64,92] The Zr K-edge spectra from $Gd_2Ti_{2-x}Zr_xO_7$ materials are shown in Figure 10.[89] As can be clearly seen, all of the spectra overlap regardless of the value of x. The lack of a significant change in the Zr K-edge XANES spectra might suggest that all Zr ions have the same coordination environment; however, the lower resolution of these spectra (relative to the Ti K-edge XANES spectra) may limit the ability of these spectra to provide accurate information on how the Zr CN changes with composition. This example represents a limitation of using K-edge XANES spectra from transition-metals located below the first-row to study CN and site occupancy changes.

<Figure 9 near here>

<Figure 10 near here>

Blanchard et al. have recently presented a study of $RE_2Zr_2O_7$ (RE = La – Tm) oxides using diffraction and XANES to study changes in the long- and short-range order of these materials, and to study the transition between the pyrochlore- and defect fluorite-type structures.[93] Unlike the Zr K-edge XANES spectra discussed above, the lower energy Zr L_3-edge XANES (2p → 4d transition) spectra are of a higher resolution, which is partly a result of the increased 2p core-hole lifetime (relative to the lifetime of the 1s core-hole), enabling a detailed analysis of how the Zr site occupancy changes depending on the rare-earth element.[94.] The Zr L_3-edge spectrum was found to be highly sensitive to changes in the local coordination environment and demonstrates an increase in local disorder across the pyrochlore oxides.[93] The double peaked nature of these spectra result from crystal field splitting of the 4d states (see Figure 11). It was demonstrated in this study that the intensity ratio of these features and the crystal field splitting energy decreased with decreasing radius of the rare-earth element (see Figure 12).[93] The increase in anti-site disorder with decreasing radius of the rare-earth ion results from the rare-earth and Zr ions becoming closer in size, which, as discussed above, is a key contributing factor to the presence of anti-site disorder. The comparison of the sensitivity between spectra from the same element (Zr in this case) but collected at different edges (K vs. L) demonstrates the need to select the appropriate edge depending on the information needed.

<Figure 11 near here>

<Figure 12 near here>

The use of glancing angle XANES (GA-XANES) to understand how radiation affects the structure of pyrochlore-type oxides

An introduction to GA-XANES

Pyrochlore-type oxides ($A_2B_2O_7$) have been investigated for nuclear waste sequestration applications due to their overall resistance to radiation-induced structural damage. Simulator elements (e.g., Ce, Zr, Gd) can be used to mimic the chemistry of actinides and ion beam implantation studies can be performed to investigate how radioactive decay damages a material.[16,50,52,55,87,95,96,97,98] It is necessary to use a technique that can selectively probe the damaged surface layer (typically only a few hundred nm thick) produced by ion beam implantation in order to investigate the resistance to radiation induced structural damage from materials.[52,53,98,99] Hard X-ray XANES spectra (> 4 KeV) are often collected to study these materials; however, these measurements are not generally surface sensitive. The surface sensitivity of these hard X-ray XANES measurements can be improved using a glancing angle geometry.[99,100,101,102] A schematic diagram for a glancing angle XANES (GA-XANES) experimental set-up is shown in Figure 13. In a GA-XANES experiment, the incident angle of the X-ray beam (generally called the glancing angle) is set to be just above the critical angle for total external reflection in order to selectively probe the surface layer. The surface sensitivity of the experiment generally increases with decreasing glancing angle.[99,100,101,102] It is demonstrated below how GA-XANES can be used to study how the local structure of pyrochlore-type oxides is affected by ion-implantation.

<Figure 13 near here>

An investigation of the structural stability of $RE_2Ti_2O_7$ pyrochlore-type oxides

In a recent study, GA-XANES spectra were collected from ion-implanted $RE_2Ti_2O_7$ (RE (rare-earth)=La-Lu, and Y), $Yb_{1.85}Ca_{0.15}Ti_2O_{7-\delta}$, and $Yb_2Ti_{1.85}Fe_{0.15}O_{7-\delta}$ materials to study how composition affects the resistance of pyrochlore-type materials to structural damage.[103] The 2 MeV Au^- ions that were implanted in the surface region of the pellets of these materials were calculated to penetrate to a maximum depth of ~450 nm in these materials (Figure 14a) with the largest number of defects being generated at a depth of ~200 nm (Figure 14b).

Ti K-edge GA-XANES spectra were collected using glancing angles that provided X-ray attenuation depths of 100 nm and 450 nm to investigate the effect of ion implantation on the local coordination environment of Ti.[103] (The change in X-ray attenuation length with glancing angle is demonstrated in Fig. 14a.) The Ti K-edge GA-XANES spectra collected at different glancing angles from $RE_2Ti_2O_7$ (RE=Sm,Gd,Yb), $Yb_2Ti_{1.85}Fe_{0.15}O_{7-\delta}$, and $Yb_{1.85}Ca_{0.15}Ti_2O_{7-\delta}$ implanted to a dose of 5×10^{14} ions/cm^2 are presented in Figure 15 and are compared to the Ti K-edge XANES spectra from the undamaged materials. It is necessary to implant proposed nuclear wasteform materials to such high doses so as to understand how these materials will respond to the decay of incorporated radioactive elements over a period of hundreds to thousands of years.[16]

The pre-edge (A) and main-edge features (B,C) in the Ti K-edge GA-XANES spectra from $RE_2Ti_2O_7$ (RE=Sm,Gd,Yb), $Yb_2Ti_{1.85}Fe_{0.15}O_{7-\delta}$, and $Yb_{1.85}Ca_{0.15}Ti_2O_{7-\delta}$ were found to change significantly upon ion implantation (Figure 15). The intensity of the pre-edge feature (A) increased while the intensity and energy of the main-edge feature (B,C) decreased as a result of ion implantation. All of these changes are a result of a decrease in the Ti CN, as a result of the

constituent ions becoming disordered in the near surface region of these materials upon Au ion implantation .[62,63,64,76,77,103]

Comparison of the GA-XANES spectra collected from the ion-implanted $RE_2Ti_2O_7$ (RE=Sm,Gd,Yb) materials using a glancing angle that provides an X-ray attenuation depth of 450 nm (Figure 16) showed that the ability of these materials to resist radiation-induced damage increased with decreasing radius of the RE cation. This conclusion was made based on the observation of a decrease in intensity of the pre-edge and an increase in the energy and intensity of the main-edge in the Ti K-edge XANES spectra from the ion-implanted materials as the RE cation was changed from Sm to Gd to Yb.[103] A similar conclusion has been made previously based on examination of electron diffraction patterns from similar ion implanted materials.[52] It has been proposed that as the radius of the RE cation decreases and approaches the radius of Ti^{4+}, the tendency for the cations to undergo anti-site disorder increases and the materials are more likely to undergo a pyrochlore to defect-fluorite phase transition because of ion implantation instead of becoming amorphous.[16,52,104] This study (along with similar studies) demonstrated the importance of the composition of a wasteform to the tolerance that these materials will have to radiation-induced structural damage.[52]

<Figure 14 near here>

<Figure 15 near here>

<Figure 16 near here>

Summary

The further development of materials for the safe sequestration of nuclear waste requires detailed information on the effect of composition, electronic structure, and the effect of the decay of radioactive elements on the long-term stability of these materials. The purpose of this contribution has been to demonstrate how XANES can be used to understand how the local structure and electronic structure of solid-state materials change depending on variations in composition, structure, and after being damaged. The ability of this technique to study materials that have long-range order, short-range order, or are amorphous demonstrates the utility of this technique and the usefulness of this technique to the investigation of solid-state materials. Although this contribution has specifically focussed on the application of XANES to the study of pyrochlore-type (and related) oxides, it should be recognized that this technique has been successfully applied to the study of a large variety of materials that have a number of applications ranging from catalysis to superconductivity to photovoltaics to nuclear materials.[103,105,106,107] Outside of demonstrating the usefulness of XANES to the study of pyrochlore-type oxides, a secondary purpose of this review has been to discuss some of the experimental considerations that must be made when using XANES to study material properties; from understanding how to control the depth sensitivity of the analysis to selecting the most appropriate edge to extract wanted information from the materials under study.

References

1. Lenzen, M., *Energies* **2010**, *3*, 462-591.
2. Lenzen, M. ,*Ener. Conver. Manage.* **2008**, *49*, 2178–2199.
3. Abu-Khader, M. M., *Prog. Nucl. Ener.* **2009**, *51*, 225–235.
4. Adamantiades, A.; Kessides, I., *Ener. Policy* **2009**, *37*, 5149–5166
5. *World energy Outlook exclusive report 2014*; International Energy Agency: Paris, 2014.
6. *The Canadian Nuclear Factbook*, Canadian Nuclear Association, **2015**.
7. *Inventory of Low-Level Radioactive Waste in Canada*, Annual Report LLRWMO-01613-041-10003; Low-level Radioactive Waste Management Office: Ottawa, 2012.
8. Manning, W. M., *J. Am. Chem. Soc.* **1962**, *84*, 315–315.
9. Ojovan, M. I.; Lee, W. E. *An Introduction to Nuclear Waste Immobilization*. Elsevier: Amsterdam, 2005.
10. Cohen, B. L., *Rev. Mod. Phys*. **1977**, *49*, 1-20.
11. Lutze, W.; Ewing, R. C., *Radioactive Waste Forms for the Future.* North Holland: Amsterdam, 1988.
12. Ewing, R. C., *Mineral. Mag.* **2011**, *75*, 2359–2377
13. Weber, W. J.; Ewing, R. C.; Angell, C. A; Arnold, G. W.; Cormack, A. N.; Delaye, J. M.; Griscom, D. L.; Hobbs, L. W.; Navrotsky, A.; Price, D. L.; Stoneham, M.; Weinberg, M. C., *J. Mater. Res*. **1997**, *12*, 1946-1978.
14. Sickafus, K. E.; Grimes, R. W.; Valdez, J. A.; Cleave, A.; Tang, M.; Ishimaru, M.; Corish, S.; Stanek, C. R.; Uberuaga, B. P., *Nature Mater.* **2007**, *6*, 217-223.
15. Weber, W. J.; Roberts, F. P. A., *Nucl. Tech.*, **1983**, *60*, 178-198.
16. Ewing, R. C.; Weber, W. J.; Lian, J., *J. Appl. Phys.* **2004**, *95*, 5949-5971.

17. Hobbs, L. W.; Sreeram, A. N.; Jesurum, C. E.; Berger, B. A., *Nucl. Instru. Meth. Phys. Res. B* **1996**, *16*, 18-25.

18. Ewing, R. C.; Chakoumakos, B.C.; Lumpkin, G. R.; Murakami, T.; Greegor, R. B.; Lytle, F. W., *Nucl. Instru. Meth. Phys. Res. B* **1988**, *32*, 487-497.

19. Lumpkin, G. R., *Elements* **2006**, *2*, 365–372.

20. Montel, J., *Comp. Rend. Geosci.* **2011**, *343*, 230–236.

21. Ewing, R. C., *Can. Mineral.* **2001**, *39*, 697-715.

22. Ewing, R. C.; Jercinovic, M. J., *MRS Proc.* **1986**, *84*, 67.

23. Clarke, D. R., *Ann. Rev. Mater. Sci.* **1983**, *13*, 191-218.

24. Wang, L.; Liang, T., *J. Adv. Ceram.* **2012**, *1*, 194-203

25. Ewing, R. C.; Weber, W. J.; Clinard, F.W., *Prog. Nucl. Energy* **1995**, *29*, 63-121.

26. Ringwood, A. E.; Oversby, V. M.; Kesson, S. E.; Sinclair, W.; Ware, N.; Hibberson, W.; Major, A., *Nucl. Chem. Waste Man.* **1981**, *2*, 287-305.

27. Ringwood, A. E.; Kesson, S. E.; Ware, N. G.; Hibberson, W. O.; Major, A., *Geochem. J.* **1979**, *13*, 141-165.

28. Ringwood, A.E.; Kesson, S.E.; Ware, N.G.; Hibberson, W.O.; Major, A., Nature 1979, 278, 219-223

29. Ringwood, A. E.; Kelly, P. M.; Bowie, S. H. U.; Kletz, T. A., *Philos. Trans. Royal Soc. London, Ser. A*, **1986**, *319*, 63-82.

30. Solomah, A. G.; Richardson, P. G.; Mcllwain, A. K., *J. Nucl. Mater.* **1987**, *148*, 157-165.

31. Solomah, A. G.; Sridhar, T. S.; Jones, S. C., *Adv. Ceram.* ***1986****, 20, 259-265.*

32. Sridhar, T. S.; Solomah, A. G., *Nucl. Tech.* **1989**, *85*, 89-97.

33. Yang, J.; Tang, B.; Luo, S., *MRS Proc.* **2000**, *663*, 333.

34. Chakoumakos, B. C., *J. Solid State Chem.* **1984**, *53*, 120-129.

35. Chakoumakos, B. C.; Ewing, R. C., *MRS Proc.* **1985**, *44*, 641-646.

36. Sohn, J. M.; Kim, M. R.; Woo, S. I., *Catal. Today* **2002**, *83*, 289-297.

37. Sarohan, P.; Hwan, H. J.; Moon, J., *Catal. Lett.* **2003**, *87,* 3–4.

38. Lee, S. H.; Yoon, C. B.; Seo, S. B.; Kim, H. E., *J. Mater. Res.* **2003**, *18*, 1765-1770.

39. Bongers, P. F.; Van Meurs, E. R., *J. Appl. Phys.* **1967**, 38, 944-945.

40. Shimakawa, Y.; Kubo, Y.; Manako, T. *Nature* **1966**, *379*, 53-55.

41. Abrantes, J. C. C.; Levchenko, A.; Shlyakhtina, A.V.; Shcherbakova, L. G.; Horovistiz, A. L.; Fagg, D. P.; Frade, J. R. *Solid State Ionics* **2006**, *177*, 1785-1788.

42. Subramanian, M. A.; Aravamudan, G.; Rao, G.V. S., *Prog. Solid State Chem.* **1983**, *15*, 55-143.

43. Todorov, I. T.; Purton, J. A.; Allan, N. L.; Dove, M. T., *J. Phys.: Condens. Matter.* **2006**, *18*, 2217–2234.

44. Momma, K.; Izumi, F., *J. Appl. Crystallogr.* **2008**, *41*, 653–658.

45. Harvey, E. J.; Whittle, K. R.; Lumpkin, G. R.; Smith, R. I.; Redfern, S. A. T., *J. Solid State Chem.* **2005**, *178*, 800–810.

46. Wang, S. X.; Begg, B. D.; Wang, L. M.; Ewing, R. C.; Weber, W. J.; Kutty, K. V. G., *J. Mater. Res.* **1999**, *14*, 4470-4473.

47. Wuensch, B. J.; Eberman, K. W.; Heremans, C.; Ku, E. M.; Onnerud, P.; Yeo, E. M. E.; Haile, S. M.; Stalick, J. K.; Jorgensen, J. D., *Solid State Ionics* **2000**, *129*, 111–133.

48. Minervini, L.; Grimes, R. W.; Sickafus, K. E., *J. Am. Ceram. Soc.* **2000**, *83*, 1873–1878.

49. Zhang, F. X.; Manoun, B.; Saxena, S. K.; Zha, C. S., *Mater. Lett.* **2006**, *60*, 2773-2776.

50. Sattonnay, G.; Moll, S.; Thomé, L.; Decorse, C.; Legros, C.; Simon, P.; Jagielski, J.; Jozwik, I.; Monnet, I., *J. Appl. Phys.* **2010**, *108*, 103512.

51. Lian, J.; Wang, L.; Chen, J.; Sun, K.; Ewing, R. C.; Farmer, J. M.; Boatner, L. A., *Acta Mater.* **2003**, *51*, 1493-1502.

52. Lian, J.; Chen, J.; Wang, L. M.; Ewing, R. C., *Phys. Rev. B* **2003**, *68*, 134107.

53. Lian, J.; Helean, K. B.; Kennedy, B. J.; Wang, L. M.; Navrotsky, A.; Ewing, R. C., *J. Phys. Chem. B* **2006**, *110*, 2343-2350.

54. Eberman, K. W., Ph.D. Thesis, Massachusetts Institute of Technology, Cambridge Massachusetts 1998.

55. Bunker, G., *Introduction to XAFS: a practical guide to X-ray absorption fine structure spectroscopy*, Cambridge University Press: Cambridge, U.K., 2010.

56. Newville, M., *Fundamentals of XAFS*, Revision 1.7.; University of Chicago: Chicago, IL, 2004.

57. De Groot, F. M. F., *Chem. Rev.* **2001**, *101*, 1779-1808.

58. Prins, R.; Koningsberger, D. C., *X-ray absorption: principles, applications, techniques of EXAFS, SEXAFS, and XANES*, Wiley: New York, 1988.

59. Grunes, L.A.; Leapman, R.D.; Wilker, C.N.; Hoffman, R.; Kunz, A.B., *Phys. Rev. B* **1982**, *25*, 7157.

60. Wilke, M.; Farges, F.; Petit, P. E.; Brown; G. E.; Martin, F., *Am. Miner.* **2001**, 86, 714-730.

61. Farges, F.; Brown, G. E.; Rehr, J. J., *Phys. Rev. B* **1997**, 56, 1809-1819.

62. Grosvenor, A. P.; Greedan, J. E., *J. Phys. Chem. C* **2009**, *113*, 11366-11372.

63. Gaultois, M. W.; Grosvenor, A. P., *J. Mater. Chem*. **2011**, *21*, 1829–1836.

64. Farges, F.; Brown, G. E.; Rehr, J. J., *Geochim. Cosmochim. Acta.* **1996**, *60*, 3023–3038.

65. Aluri, E. R.; Grosvenor, A. P. , *J. Phys. Chem. Solids*, 2013, **74**, 830 – 836.

66. Aluri, E. R.; Grosvenor, A. P., *Phys. Chem. Chem. Phys.*, **2013**, 15, 10477 – 10486.

67. Horovisitz, A.L.; Fagg, D.P.; Abrantes, J.C.C.; Frade, J.R., J. Eur. Ceram. Soc. 2007, 27, 4283–4286.

68. Elfimov, I.S.;. Anisimov, V.I; Sawatzky, G.A., Phys. Rev. Lett. 1999, 82, 4264.

69. Gaultois, M.W., Grosvenor, A.P., J. Phys. Chem. C 2010, 114, 19822-19829.

70. Berlier, G.; Spoto, G.; Bordiga, S.; Ricchiardi, G.; Fisicaro, P.; Zecchina, A.; Rossetti, I.; Selli, E.; Forni, L.; Giamello, E.; Lamberti, C., J. Catal. 2002, 208, 64–82.

71. Le Toquin, R.; Paulus, W.; Cousson, A.; Prestipino, C.; Lamberti, C., J. Am. Chem. Soc. 2006, 128, 13161–13174.

72. Haas, O.; Vogt, U.F.; Soltmann, C.; Braun, A.; Yoon, W.S.; Yang, X.Q.; Graule, T., Mater. Res. Bull. 2009, 44, 1349-1404.

73. Yamamoto, T., *X-Ray Spectrom*, 2008, **37**, 572–584.

74. Cabaret, D.; Bordage, A.; Juhin, A.; Arfaoui M.; Gaudry, E., *Phys. Chem. Chem. Phys.,* 2010, **12**, 5619–5633.

75. Cabaret, D.; Joly, Y.; Renevier H.; Natoli, C.R., *J. Synchrotron Rad*., 1999, **6**, 258–260.

76. Waychunas, G. A., *Am. Mineral.*, 1987, **72**, 89 – 101.

77. Farges, F.; Brown, G. E. Jr.; Rehr, J. J., *Phys. Rev. B*, 1997, **56**, 1809-1819.

78. T. H. Yu, Ph.D. Thesis, Massachusetts Institute of Technology, Cambridge, Massachusetts, 1996.

79. Sigrist, J. A.; Gaultois, M. W.; Grosvenor, A. P., *J. Phys. Chem. A,* 2011, **115**, 1908–1912.

80. van Bokhoven, J. A.; Nabi, T.; Sambe, H.; Ramaker D. E.; Koningsberger, D. C., *J. Phys.: Condens. Matter*, 2001, **13**, 10247 – 19260.

81. Allred, A. L.; Rochow, E. G., *J. Inorg. Nucl. Chem.* 1958, **5**, 264-268.

82. Guillot, F.; Dézarnaud-Dandine, C.; Tronc, M., *Chem. Phys.* 1997, **224**, 281-300.

83. Liu, Z.; Handab, K.; Kaibuchi, K.; Tanaka, Y.; Kawai, J., *J. Electron Spectrosc. Relat. Phenom.* 2004, **135**, 155–158.

84. Akatsuka, T.; Ushiro, M.; Nagamatsu, S.; Takahashi, Y.; Fujikawa, T., *Polyhedron* 2008, **27**, 3146-3150.

85. Nachimuthu, P.; Thevuthasan, S.; Adams, E. M.; Weber, W. J.; Begg, B. D.; Mun, B. S.; Shuh, D. K.; Lindle, D. W.; Gullikson, E. M.; Perera, R. C. C., *J. Phys. Chem. B* 2005, 109, 1337 – 1339.

86. Moreno, K. J.; Fuentes, A. F.; Maczka, M.; Hanuza, J.; Amador, U, *J. Solid State Chem.* 2006, 179, 3805-3813.

87. Zhang, J.; Lian, J.; Zhang, F.; Wang, J.; Fuentes, A. F.; Ewing, R. C., *J. Phys. Chem. C* 2010, 114, 11810 – 11815.

88. Shannon, R. D., *Acta Cryst.*, 1976, A32, 751 – 767.

89. Walker, J. D. S.; Hayes, J. R.; Gaultois, M. W.; Aluri, E. R.; Grosvenor, A. P., *J. Alloys Compd.*, 2013, **565**, 44 – 49.

90. Joly, Y., Cabaret, D., Renevier, H., Natoli, C. R., *Phys. Rev. Lett.* 1999, 82, 2398 – 2401.

91. Mountjoy, G.; Pickup, D. M.; Anderson, R.; Wallidge, G. W.; Holland, M. A.; Newport, R. J.; Smith, M. E., *Phys. Chem. Chem. Phys.* 2000, 2, 2455 – 2460.

92 Gaultois, M. W.; Grosvenor, A. P., *Phys. Chem. Chem. Phys.* 2012, 14, 205 – 217.

93. Blanchard, P. E. R.; Clements, R.; Kennedy, B. J.; Ling, C. D.; Reynolds, E.; Avdeev, M.; Stampfl, A. P. J.; Zhang, Z., *Inorg. Chem.* **2012**, 51, 13237 – 13244.

94. Krause, M. O.; Oliver, J. H., J. Phys. Chem. Ref. Data, 1979, 8, 329 – 338.

95. Robin, T. *Reprocessing and Recycling of Spent Nuclear Fuel*; Elsevier: Cambridge, 2015.

96. US Nuclear Regulatory Commission. http://www.nrc.gov/waste/spent-fuel-storage/pools.html

97. Strachan, D. M.; Scheele, R. D.; Buck, E. C.; Icenhower, J. P.; Kozelisky, A. E.; Sell, R. L.; Elovich, R. J.; Buchmiller, W. C., *J. Nucl. Mater.* **2005**, *345*, 109–135.

98. Lian, J.; Zu, X. T.; Kutty, K. V. G.; Chen, J.; Wang, L. M.; Ewing, R. C., *Phys. Rev. B* **2002**, *66*, 054108.

99. Reid, D. P.; Stennett, M. C.; Ravel, B.; Woicik, J. C.; Peng, N.; Maddrell, E. R.; Hyatt, N. C., *Nucl. Instrum. Meth. Phys. Res. B* **2010**, *268*, 1847-1852.

100. Greaves, G. N.; Barrett, N. T.; Antonini, G. M.; Thornley, F. R.; Willis, B. T. M.; Steel, A., *Am. Chem. Soc.* **1989**, *111*, 4313-4324.

101. Waychunas, G. A., *Rev. Mineral. Geo. Chem.* **2002**, *49*, 267-315.

102. England, K. E. R.; Charnock, J. M.; Pattrick, R. A. D.; Vaughan, D. J., *Mineral. Mag.* **1999**, *63*, 559-566.

103. Aluri, E. R.; Grosvenor, A. P., *J. Alloys Compd.*, **2014**, 616, 516 – 526.

104. Zhang, Z.L.; Xiao, H.Y.; Zu, X.T.; Gao, F.; Weber, W.J., J. Mater. Res. 2009, 24, 1335-1341.

105. Aluri, E.R.; Hayes, J.R.; Walker, J.D.S.; Grosvenor, A.P., *J. Phys. Chem. C* 2014, 15, 7910–7922.

106. Booth, C. H.; Durakiewicz, T.; Capan, C.; Hurt, D.; Bianchi, A. D.; Joyce, J. J.; Fisk, Z., *Phys. Rev. B*, **2011**, 83, 235117

107. Dadlani, A. L.; Acharya, S.; Trejo, O.; Prinz, F. B.; Torgersen, J., *ACS Appl. Mater. Interfaces*, **2016**, 8, 14323 – 14327.

Figure captions:

Figure 1: A portion of the unit cell (1/8) of the pyrochlore-type structure of $A_2B_2O_7$ is shown. The structure consists of AO_8 in distorted cubic polyhedra (dark grey), distorted BO_6 octahedra (light grey), and O atoms (dark grey spheres) occupy tetrahedral interstitial sites.

Figure 2: A representative energy diagram for transitions observed in K- and L-edge XANES spectra from first-row transition metals is shown.

Figure 3: (a) Ti K-edge XANES speactra from materials having 4-coordinate (Ba_2TiO_4), 5-coordinate ($Ba_2TiSi_2O_8$), and 6-coordinate ($Gd_2Ti_2O_7$) Ti^{4+}. The intensity and energy of pre-edge peak (A) are observed to change significantly with varying CN. These changes are also accompanied by changes in the main-edge features (B,C). (b) Ti K-edge XANES speactra from TiO_2 (Ti^{4+})and Ti_2O_3 (Ti^{3+}) are presented to demonstrate the energy shift observed with increaseing oxidation state.

Figure 4: Fe K-edge XANES spectra from the $Yb_2Ti_{2-x}Fe_xO_{7-\delta}$ system. Feature A represents the pre-edge region (1s→3d excitations) while features B and C represent the main-edge region (1s→4p transitions). The pre-edge region (Feature A) of the spectra from $Yb_2Ti_{2-x}Fe_xO_{7-\delta}$ is shown in the inset. The changes in intensity or energy of features A, B and C with increasing Fe content are marked by arrows. Reprinted from Journal of Physics and Chemistry of Solids, 74, E. R. Aluri, A. P. Grosvenor, An investigation of pyrochlore-type oxides ($Yb_2Ti_{2-x}Fe_xO_{7-\delta}$) by XANES, 830 – 836 (2013), with permission from Elsevier.

Figure 5: The pre-edge region from the Fe K-edge XANES spectra for $Yb_2Ti_{2-x}Fe_xO_{7-\delta}$ (x=0.05, 0.10), $LaFeO_3$, and $SrFeO_3$ are presented. The energies of the pre-edge peaks from all spectra from $Yb_2Ti_{2-x}Fe_xO_{7-\delta}$ are equivalent to that from the spectrum from $LaFeO_3$. Reprinted from

Journal of Physics and Chemistry of Solids, 74, E. R. Aluri, A. P. Grosvenor, An investigation of pyrochlore-type oxides ($Yb_2Ti_{2-x}Fe_xO_{7-\delta}$) by XANES, 830 – 836 (2013), with permission from Elsevier.

Figure 6: (a) Ti K-edge XANES spectra from the $Gd_2Ti_{2-x}Sn_xO_7$ system. Feature A (A_1, A_2, and A_3) represents the pre-edge region (1s→3d) whereas features B and C represent the main-edge region (1s→4p). The pre-edge region is shown in the inset and arrows mark the changes observed in the spectra with increasing Sn content. (b) The first derivative of the Ti K-edge XANES spectra from $Gd_2Ti_{2-x}Sn_xO_7$ are shown. The vertical dashed lines represent the peak energies of feature B from the $Gd_2Ti_{2-x}Sn_xO_7$ series when x = 0.0 and 1.5. Reprinted from E. R. Aluri, A. P. Grosvenor, Phys. Chem. Chem. Phys. **2013**, *15*, 10477 with permission from the Royal Society of Chemistry.

Figure 7: (a) The partial DOS calculations of the Ti 4p states from $Y_2Ti_{2-x}Sn_xO_7$ are plotted relative to the Fermi-level (0 eV). The vertical dashed lines represent the positive shift in energy (~+0.8 eV) observed with increasing Sn content. (b) The Ti 3d partial DOS calculations from $Y_2Ti_{2-x}Sn_xO_7$ are presented and were observed to shift by ~ -0.3 eV with increasing Sn incorporation. Reprinted from E. R. Aluri, A. P. Grosvenor, Phys. Chem. Chem. Phys. **2013**, *15*, 10477 with permission from the Royal Society of Chemistry.

Figure 8: The Sn L_3-edge XANES spectra from $Gd_2Ti_{2-x}Sn_xO_7$ are presented. Feature A and B result from $2p_{3/2}$→4s and $2p_{3/2}$→5d transitions and Feature C (~3960 eV) results from multi-scattering resonances. Arrows mark the changes in intensity and absorption energy of features A, B, and C with increasing Sn concentration. Reprinted from E. R. Aluri, A. P.

Grosvenor, Phys. Chem. Chem. Phys. **2013**, *15*, 10477 with permission from the Royal Society of Chemistry.

Figure 9: Ti K-edge XANES spectra from the $Gd_2Ti_{2-x}Zr_xO_7$ materials. Reprinted from Journal of Alloys and Compounds, 565, J. D. S. Walker, J. R. Hayes, M. W. Gaultois, E. R. Aluri, A. P. Grosvenor, A case for oxygen deficiency in $Gd_2Ti_{2-x}Zr_xO_7$ pyrochlore-type oxides, 44 – 49 (2013), with permission from Elsevier.

Figure 10: a) Zr K-edge XANES spectra from some of the $Gd_2Ti_{2-x}Zr_xO_7$ materials studied are presented. Very little change in the spectra was observed with varying Zr concentration. Reprinted from Journal of Alloys and Compounds, 565, J. D. S. Walker, J. R. Hayes, M. W. Gaultois, E. R. Aluri, A. P. Grosvenor, A case for oxygen deficiency in $Gd_2Ti_{2-x}Zr_xO_7$ pyrochlore-type oxides, 44 – 49 (2013), with permission from Elsevier.

Figure 11: Fitted Zr L_3-edge XANES spectra from (a) $La_2Zr_2O_7$ and (b) $Tm_2Zr_2O_7$, are presented. The Zr L_3-edge spectra were fitted to extract information on the Zr 4d crystal field splitting energy (ΔE) and to understand how the peak areas change depending on composition. Reprinted with permission from P. E. R. Blanchard, R. Clements, B. J. Kennedy, C. D. Ling, E. Reynolds, Inorg. Chem. **2012**, *51*, 13237 – 13244. Copyright (2012) American Chemical Society.

Figure 12: Plots of the crystal field splitting (ΔE) and the A:B intensity ratio ($I_A/(I_{B1} + I_{B2})$) extracted from the fitted Zr L_3-edge XANES spectra vs. the ionic radius ratio between the rare-earth (r_{Ln}; i.e., r_A) and Zr (r_{Zr}; i.e., r_B) are presented. Reprinted with permission from P. E. R. Blanchard, R. Clements, B. J. Kennedy, C. D. Ling, E. Reynolds, Inorg. Chem. **2012**, *51*, 13237 – 13244. Copyright (2012) American Chemical Society.

Figure 13: The experimental set up used to collect glancing angle XANES spectra using the 20BM beamline at the Advanced Photon Source is shown.

Figure 14: (a) A plot of the Au^- ion beam implantation depth profile from $Yb_2Ti_2O_7$ calculated using SRIM-2013 is shown. A plot of glancing angle *versus* X-ray attenuation depth for $Yb_2Ti_2O_7$ is also shown and was calculated for photons having an energy of 4966 eV (Ti K-edge). (b) A plot of the number of vacancies produced per Au^- ion (defect-per-ion profile) in $Yb_2Ti_2O_7$ is presented. Reprinted from Journal of Alloys and Compounds, 616, E. R. Aluri, A. P. Grosvenor, An investigation of the electronic structure and structural stability of $RE_2Ti_2O_7$ by glancing angle and total electron yield XANES, 516 – 526 (2014), with permission from Elsevier.

Figure 15: Ti K-edge GA-XANES spectra collected at various glancing angles from (a) $Sm_2Ti_2O_7$, (b) $Gd_2Ti_2O_7$, (c) $Yb_2Ti_2O_7$, (d) $Yb_2Ti_{1.85}Fe_{0.15}O_{7-\delta}$, and (e) $Yb_{1.85}Ca_{0.15}Ti_2O_{7-\delta}$ implanted to a dose of 5×10^{14} ions/cm^2 are shown along with the spectra from the undamaged samples. The glancing angles used were chosen to attain X-ray attenuation depths of 100 nm and 450 nm. Arrows indicate the changes observed in features A-C in the spectra with decreasing glancing angle. Reprinted from Journal of Alloys and Compounds, 616, E. R. Aluri, A. P. Grosvenor, An investigation of the electronic structure and structural stability of $RE_2Ti_2O_7$ by glancing angle and total electron yield XANES, 516 – 526 (2014), with permission from Elsevier.

Figure 16: Ti K-edge GA-XANES spectra from the implanted $(Sm,Gd,Yb)_2Ti_2O_7$ materials collected using a glancing angle that provided an X-ray attenuation depth of 450 nm are shown. Arrows mark the changes observed in the spectra as the RE was changed from Sm to Gd to Yb.

All materials were implanted with 2 MeV Au^- ions to a dose of 5 x 10^{14} ions/cm^2. Reprinted from Journal of Alloys and Compounds, 616, E. R. Aluri, A. P. Grosvenor, An investigation of the electronic structure and structural stability of $RE_2Ti_2O_7$ by glancing angle and total electron yield XANES, 516 – 526 (2014), with permission from Elsevier.

Figures:

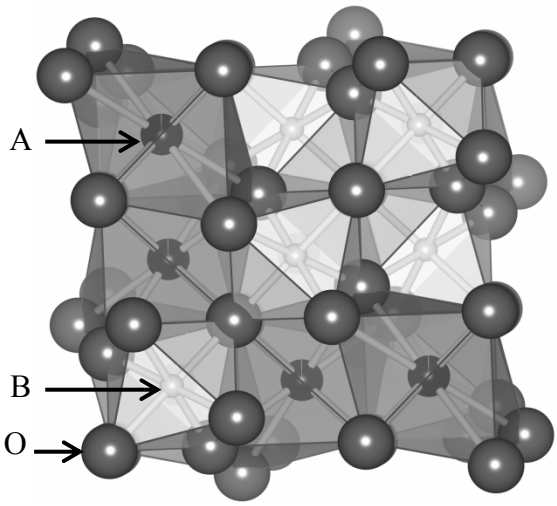

Figure 1

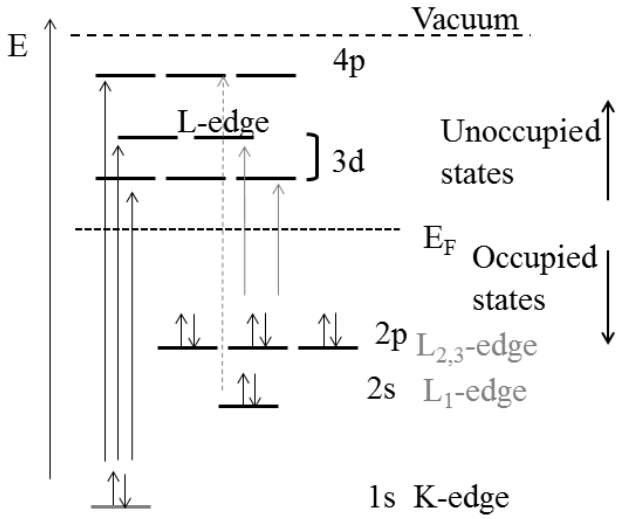
E
Vacuum
4p
L-edge
3d
Unoccupied
states
E_F
Occupied
states
2p
$L_{2,3}$-edge
2s
L_1-edge
1s K-edge

Figure 2

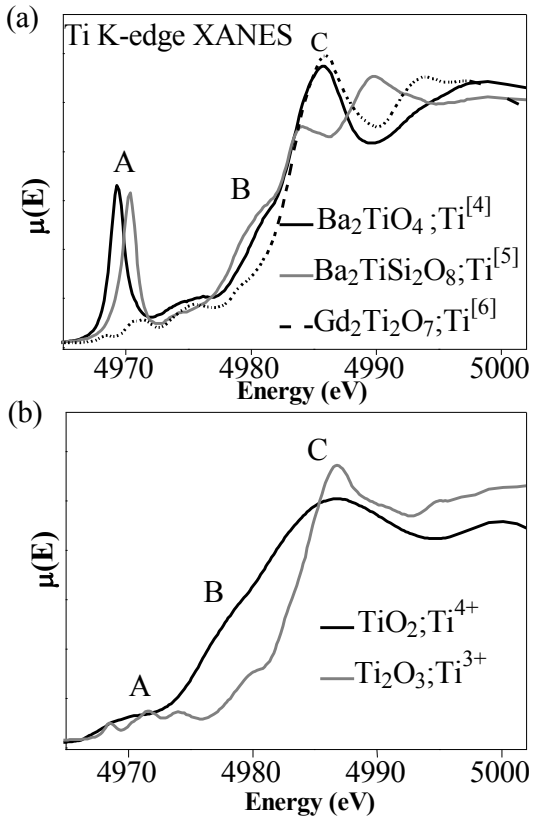
(a)
Ti K-edge XANES
A
B
C
μ(E)
Ba2TiO4 ;Ti[4]
Ba2TiSi2O8;Ti[5]
Gd2Ti2O7;Ti[6]
4970
4980
4990
5000
Energy (eV)
(b)
A
B
C
μ(E)
TiO2;Ti4+
Ti2O3;Ti3+
4970
4980
4990
5000
Energy (eV)

Figure 3

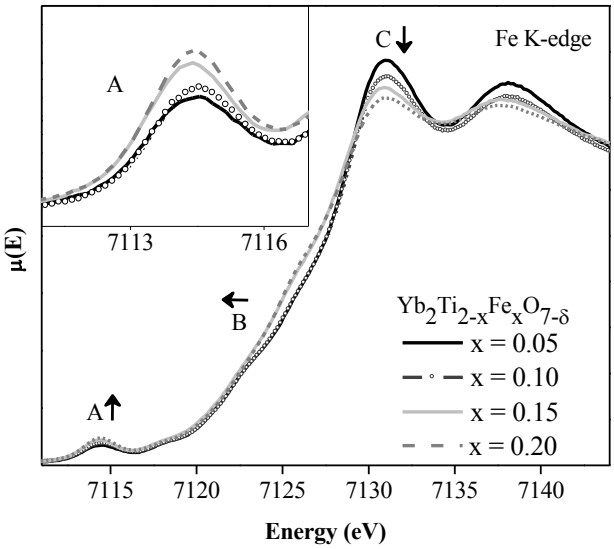
A
C
Fe K-edge
7113
7116
μ(E)
B
A
$Yb_2Ti_{2-x}Fe_xO_{7-\delta}$
x = 0.05
x = 0.10
x = 0.15
x = 0.20
7115
7120
7125
7130
7135
7140
Energy (eV)

Figure 4

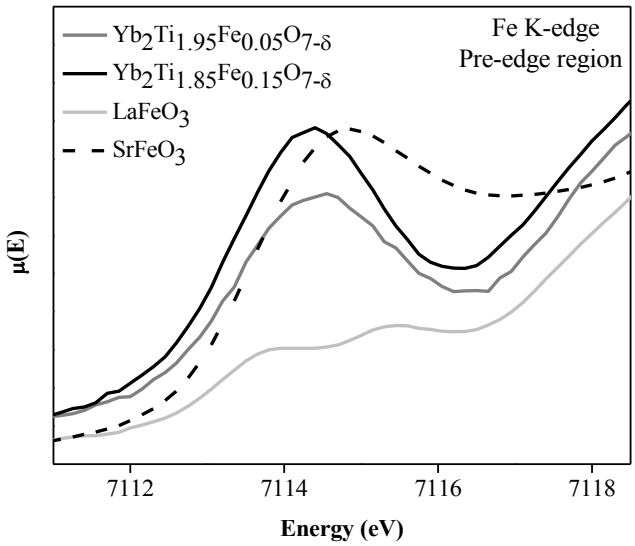
Yb2Ti1.95Fe0.05O7-δ
Yb2Ti1.85Fe0.15O7-δ
LaFeO3
SrFeO3
Fe K-edge
Pre-edge region
μ(E)
7112
7114
7116
7118
Energy (eV)

Figure 5

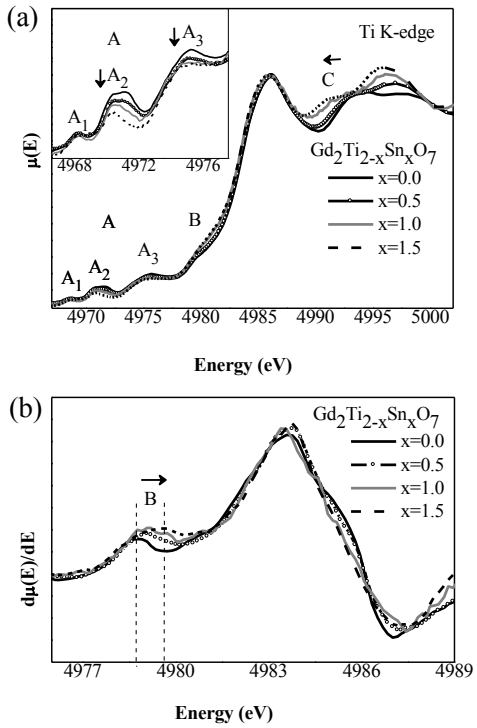
(a)
Ti K-edge
A
A3
A2
A1
C
μ(E)
Gd2Ti2-xSnxO7
x=0.0
x=0.5
x=1.0
x=1.5
A
B
A3
A1
A2
4970
4975
4980
4985
4990
4995
5000
4968
4972
4976
Energy (eV)
(b)
Gd2Ti2-xSnxO7
x=0.0
x=0.5
x=1.0
x=1.5
B
dμ(E)/dE
4977
4980
4983
4986
4989
Energy (eV)

Figure 6

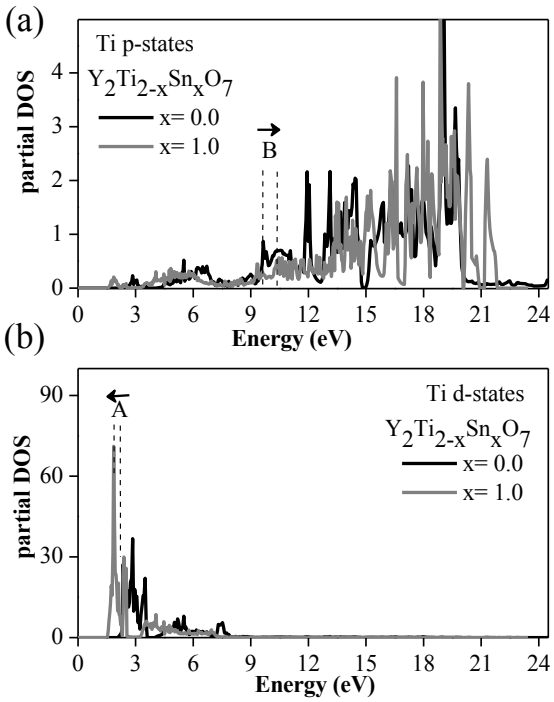
(a)
Ti p-states
$Y_2Ti_{2-x}Sn_xO_7$
x= 0.0
x= 1.0
B
partial DOS
Energy (eV)
(b)
Ti d-states
$Y_2Ti_{2-x}Sn_xO_7$
x= 0.0
x= 1.0
A
partial DOS
Energy (eV)

Figure 7

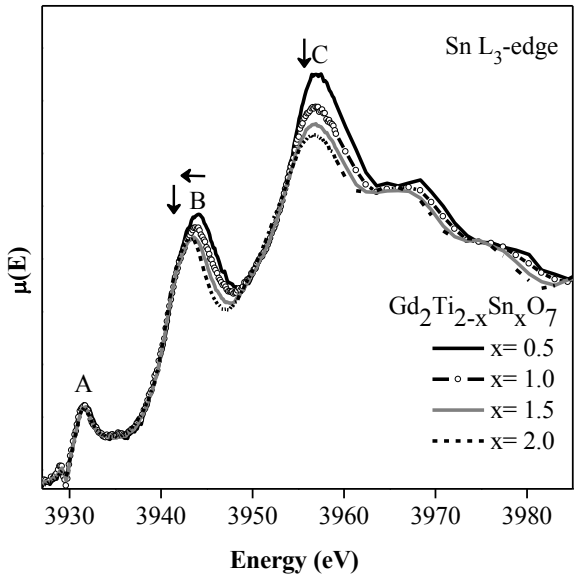
Sn L3-edge
C
B
A
μ(E)
Gd2Ti2-xSnxO7
x= 0.5
x= 1.0
x= 1.5
x= 2.0
3930
3940
3950
3960
3970
3980
Energy (eV)

Figure 8

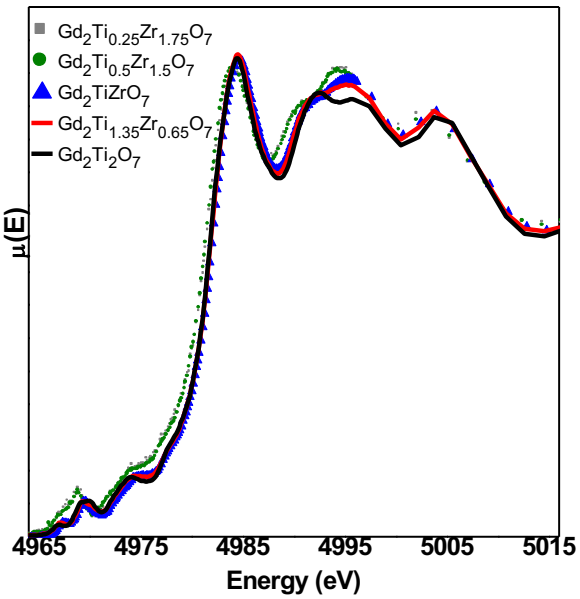
Gd2Ti0.25Zr1.75O7
Gd2Ti0.5Zr1.5O7
Gd2TiZrO7
Gd2Ti1.35Zr0.65O7
Gd2Ti2O7
μ(E)
4965
4975
4985
4995
5005
5015
Energy (eV)

Figure 9

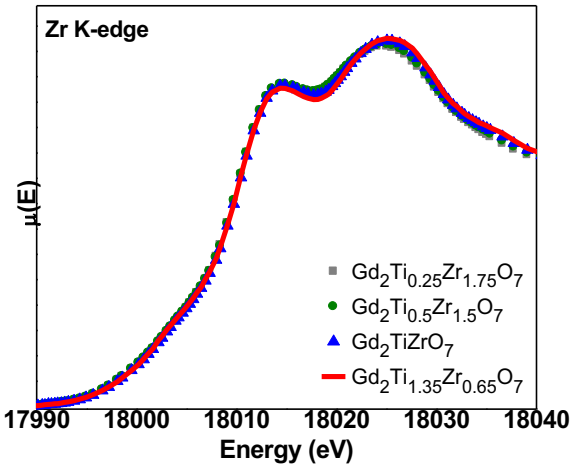
Zr K-edge
μ(E)
Gd2Ti0.25Zr1.75O7
Gd2Ti0.5Zr1.5O7
Gd2TiZrO7
Gd2Ti1.35Zr0.65O7
17990
18000
18010
18020
18030
18040
Energy (eV)

Figure 10

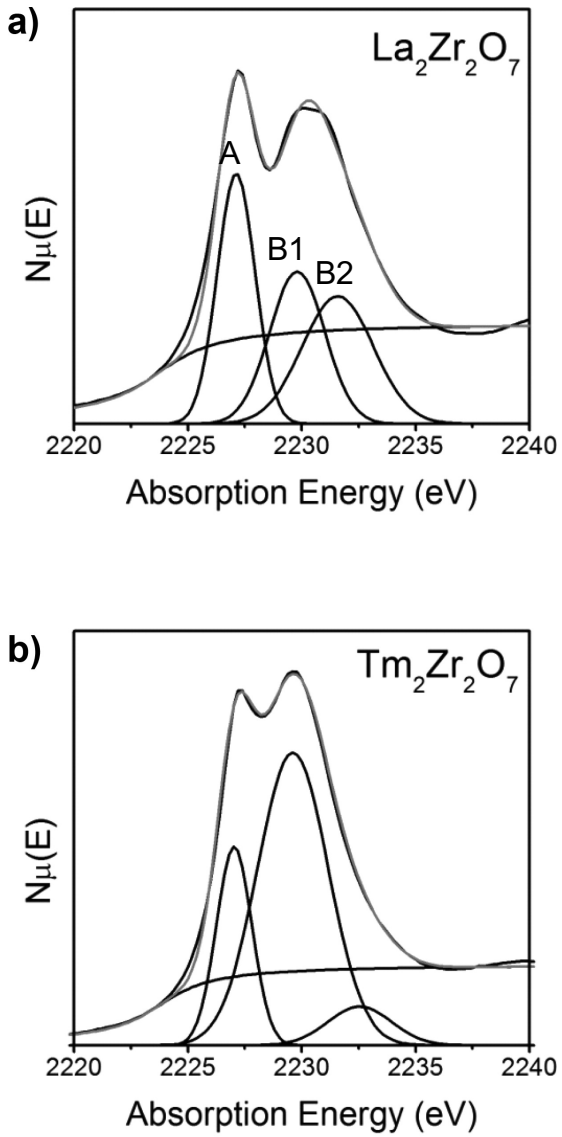
a)
$La_2Zr_2O_7$
A
B1
B2
Nμ(E)
2220
2225
2230
2235
2240
Absorption Energy (eV)
b)
$Tm_2Zr_2O_7$
Nμ(E)
2220
2225
2230
2235
2240
Absorption Energy (eV)

Figure 11

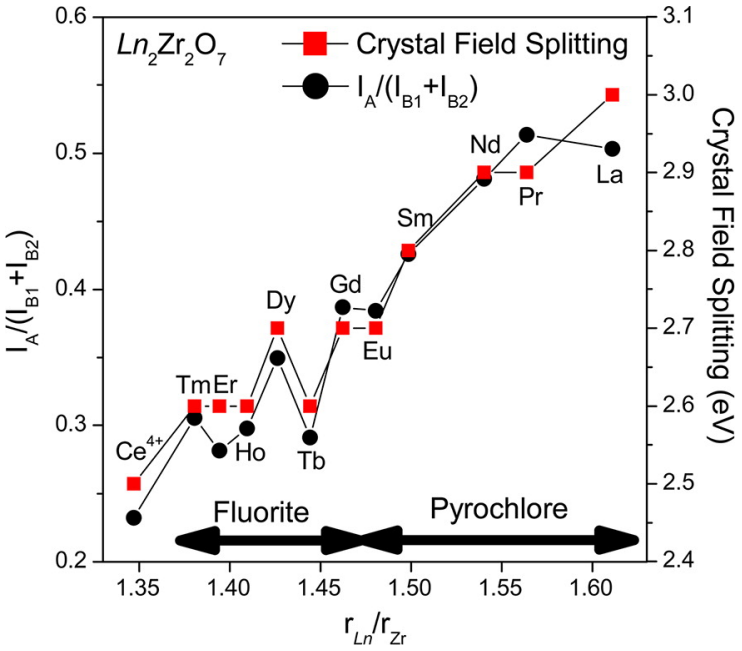
$Ln_2Zr_2O_7$
Crystal Field Splitting
$I_A/(I_{B1}+I_{B2})$
Crystal Field Splitting (eV)
$I_A/(I_{B1}+I_{B2})$
r_{Ln}/r_{Zr}
Ce4+
Tm
Er
Ho
Dy
Tb
Gd
Eu
Sm
Nd
Pr
La
Fluorite
Pyrochlore

Figure 12

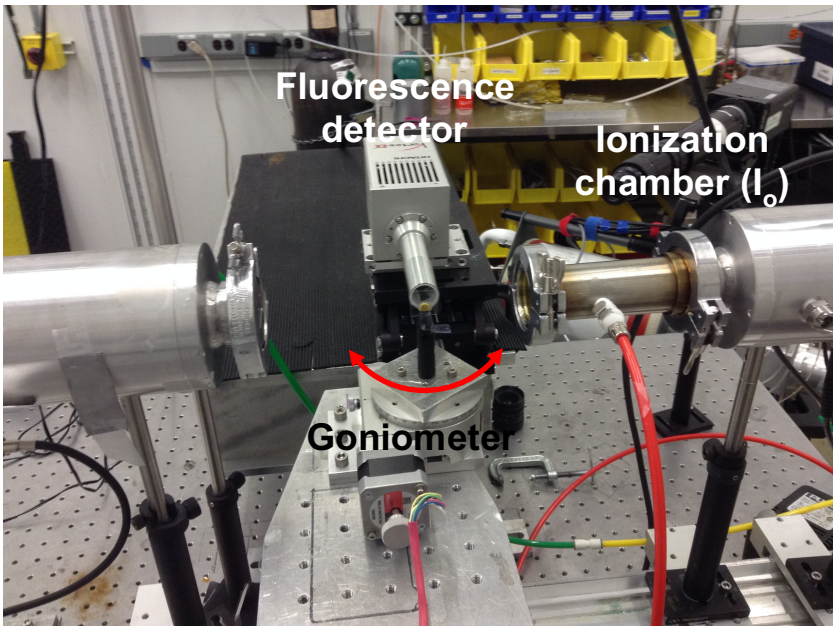

Figure 13

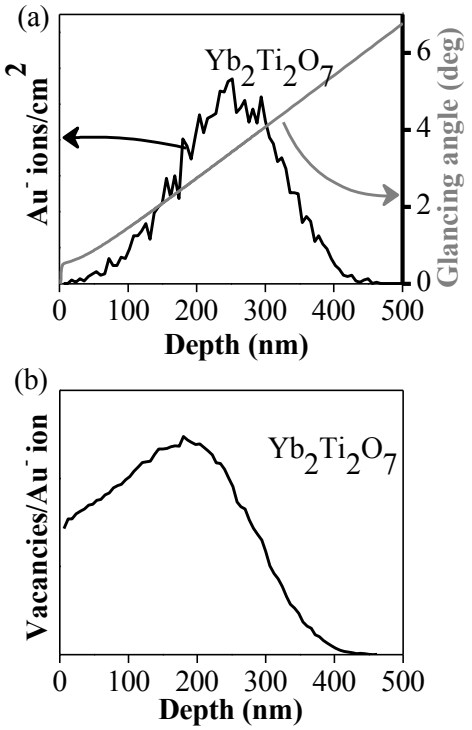
(a)
Au⁻ ions/cm²
Yb2Ti2O7
Glancing angle (deg)
0
2
4
6
0
100
200
300
400
500
Depth (nm)
(b)
Vacancies/Au⁻ ion
Yb2Ti2O7
0
100
200
300
400
500
Depth (nm)

Figure 14

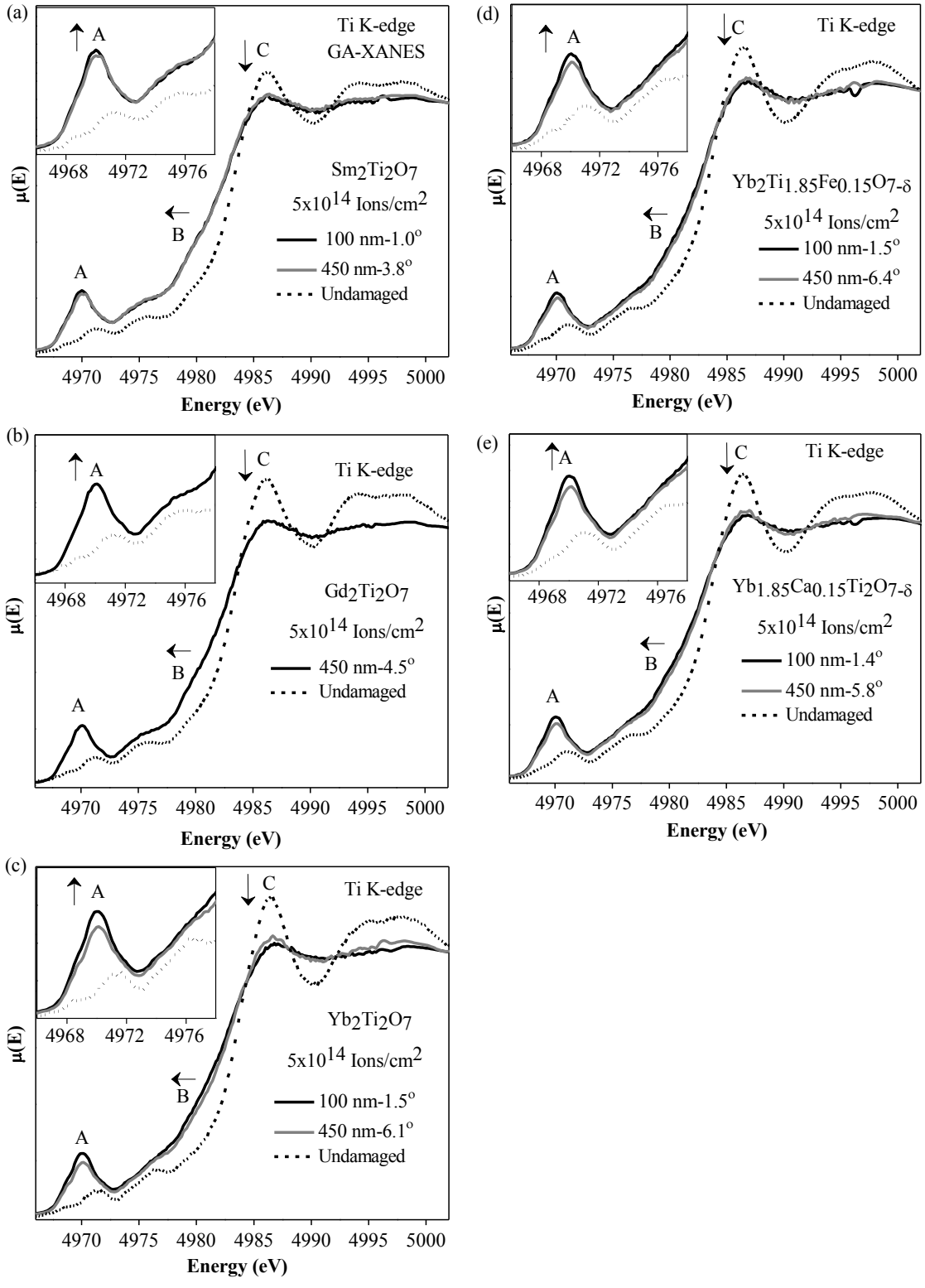
(a)
Ti K-edge
GA-XANES
A
B
C
$Sm_2Ti_2O_7$
$5x10^{14}$ Ions/cm^2
100 nm-1.0°
450 nm-3.8°
Undamaged
μ(E)
Energy (eV)
(b)
Ti K-edge
$Gd_2Ti_2O_7$
$5x10^{14}$ Ions/cm^2
450 nm-4.5°
Undamaged
(c)
Ti K-edge
$Yb_2Ti_2O_7$
$5x10^{14}$ Ions/cm^2
100 nm-1.5°
450 nm-6.1°
Undamaged
(d)
Ti K-edge
$Yb_2Ti_{1.85}Fe_{0.15}O_{7-\delta}$
$5x10^{14}$ Ions/cm^2
100 nm-1.5°
450 nm-6.4°
Undamaged
(e)
Ti K-edge
$Yb_{1.85}Ca_{0.15}Ti_2O_{7-\delta}$
$5x10^{14}$ Ions/cm^2
100 nm-1.4°
450 nm-5.8°
Undamaged
4968 4972 4976
4970 4975 4980 4985 4990 4995 5000

Figure 15